Studies of Electron Collisions with CN^+, CN^- and HCN^+/HNC^+

Arnaud Le Padellec
LCAR UMR 5589, Université Paul Sabatier-Toulouse III, 118 route de Narbonne, Bât. III R1B4, 31062 Toulouse Cedex 4, France
arnaud.lepadellec@irsamc.ups-tlse.fr

1. INTRODUCTION

We made use of two different merged beam setups, MEIBE and CRYRING to study electron collisions upon molecular ions. Absolute cross sections and branching fractions over the final product states were measured for the dissociative recombination (DR) of $CN^+(X^1\Sigma^+$ and $^3\Pi$, v=0). The same process was investigated for isomeric HCN^+/HNC^+ target ions. An isomeric mixture was first studied, and HNC^+ was then almost exclusively isolated. The two sets of measurements exhibit differences and the process is found to be overwhelmingly more efficient for HCN^+ than that for HNC^+. Electrons were also scattered on CN^- ($X^1\Sigma^+$, v=0, 1) target ions. Pure detachment is found to dominate over fragmentation channels. The cross section curve rises from threshold near 7 eV, up to a plateau.

2. MERGED BEAM SINGLE PASS APPARATUS: MEIBE

A sketch of the single pass merged beam (MEIBE) set-up is presented in Fig. 1. The ions are produced in a radio frequency ion source mounted in the terminal of a 400keV Van de Graaff accelerator. After mass analysis, the ion beam is injected into the collision chamber where a beam of electrons, produced by a barium oxide cathode, is merged with it using a combination

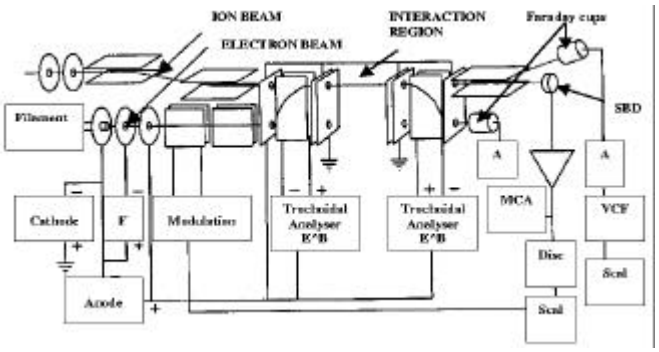

Figure 1. A sketch of the MEIBE apparatus at the University of Western Ontario. The ions come from the top left. Both trochoidal analyzers (entrance and exit of the 8.6cm interaction region) in which the electrons display jumps, are indicated.

of transverse electric and magnetic fields in a trochoidal analyzer. The beams interact with each other over a distance of 8.6 cm. After the interaction region, the electrons are de-merged, the electron beam collected and measured in a Faraday cup, which is connected to a Keithley electrometer. The ion beam is deflected electrostatically into another Faraday cup, also connected to an electrometer. Fast neutrals, formed in the interaction region continue undeflected on their original path, to be detected further downstream by an energy sensitive surface barrier detector. Recently, we performed a careful reanalysis of the quantum efficiency of our detector and this was indeed, found to be essentially unity.

2.1 Signal Analysis

The true recombination signal is extracted from the background arising from charge exchange collisions by modulating the electron beam and counting the signals in and out of phase with the modulation. Since the simultaneous arrival of two or three neutral particles is indistinguishable from that of a single particle having the same total mass, the DR signal appears in the "full energy" channel. This can be selected for counting using a single channel analyzer (SCA), with lower and upper gating levels set accordingly. The overlap of the two beams in the interaction region is monitored using moveable scanners and the effective collision area, F, determined.[1] The electron and ion currents, I_e and I_i, the electron and ion velocities in the laboratory frame, v_e and v_i, as well as the neutral signal count rate, C_n, are all measured.

The cross section $\sigma(v_{cm})$ is given by:

$$\sigma(v_{cm}) = \frac{C_n}{I_i}\frac{e^2}{I_e}\frac{F}{L}\left|\frac{v_i \cdot v_e}{v_i - v_e}\right| \tag{1}$$

where e is the elementary charge. The conventional relation gives the center of mass (CM) energy:

$$E_{cm} = \left(\sqrt{E_+} - \sqrt{E_e}\right)^2 \tag{2}$$

where $E_+=(m_e/m_i)E_i$ is the reduced collision energy and E_e is the electron energy. Another important issue is the energy resolution of the MEIBE apparatus. Although we make use of Eq. 1 in order to determine the recombination cross section, one must take into account the finite energy resolution of the apparatus. The measurements yield an average of a velocity weighted cross section over a "flattened" anisotropic electron velocity distribution, f:

$$f(v_e) = \frac{m_e}{2\pi k T_{e\perp}}\left(\frac{m_e}{2\pi k T_{e//}}\right)^{1/2} \exp\left(-\frac{m_e v_{e\perp}^2}{2kT_{e\perp}} - \frac{m_e v_{e//}^2}{2kT_{e//}}\right) \tag{3}$$

(where $T_{e//}$ and $T_{e\perp}$ represent the longitudinal and transverse temperatures, respectively) according to:

$$\left\langle \sigma(v_{rel}) v_{rel} \right\rangle = \int_{-\infty}^{+\infty} v_{rel}\sigma(v_{rel}) f(v_e) d^3 v_e \tag{4}$$

which for small values of the energy resolution compared to the CM energy, can be simplified to:

$$\left\langle \sigma(v_{rel}) v_{rel} \right\rangle = \sigma(v_{cm}) v_{cm} . \tag{5}$$

In order to check the validity of our simplification, we extracted the rate coefficients $\left\langle \sigma(v_{rel}) v_{rel} \right\rangle$ from our measured cross sections at specific v_{cm} values for HCN^+,[2] and we then applied a Fourier transform based technique[3]:

$$\sigma(v_{cm}) = \frac{1}{v_{cm}} F^{-1}\left[\frac{F\left(\left\langle \sigma(v_{rel}) v_{rel} \right\rangle\right)}{F(f)}\right] \tag{6}$$

which is similar to that used in the storage ring community to extract the cross section from the rate coefficient $\left\langle \sigma(v_{rel}) v_{rel} \right\rangle$. F represents the Fourier Transform and f is the electron velocity distribution defined above. The

assumption was made that the longitudinal electron temperature is negligible compared to the transverse one. This assumption has been shown to be valid in several circumstances.[4,5] The deconvoluted cross sections obtained are essentially those obtained directly from Eq.(1) and we therefore confirm the high energy resolution of our apparatus.

3. MERGED BEAM MULTI-PASS APPARATUS: HEAVY ION STORAGE RING CRYRING

The storage ring CRYRING is displayed in Fig. 2.

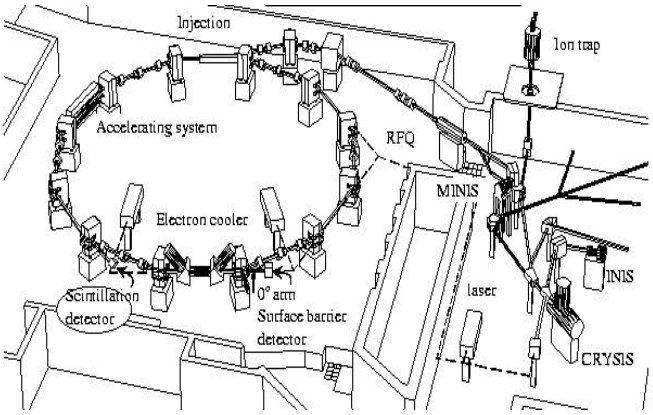

Figure 2. A view of the heavy ion storage ring CRYRING (Manne Siegbahn Institute - Stockholm University).

3.1 Rate Coefficient Determination

Each machine cycle consists of five phases: injection (following extraction (usually at 40 keV) from the ion source), acceleration, cooling, measurement and dumping of the beam. About one second is used for the two first phases. The relatively long storage time of the ions in the ring makes possible, in most cases, the relaxation of their internal degrees of freedom prior to measurement (the so-called "cooling" phase). By varying the electron velocity, collisions at different CM energies, E_{cm}, can be achieved, and this is given by an equation similar to Eq.(2). Various types of measurement protocols can be used. The CM energy can be varied either by jumping or ramping continuously the electron cooler cathode voltage. Three different types of detectors are used during the experiments: two are used for the monitoring of the ion beam during the recording of data and one is used to

record the events from the process under study. A current transformer is used for an absolute ion current measurement. A drawback is its relatively low sensitivity and hence both a large ion beam and long integration times are required in order to get a statistically acceptable measurement. Another detector, a scintillator, monitors the ion current and is placed after one of the straight sections. It monitors the background associated with the neutralization of the ions in the beam, due to collisions with the rest gas. This detector has a large dynamical range but it cannot be used for an absolute cross section measurement since the signal depends on the pressure in the vacuum chamber. Energy sensitive surface barrier detectors (SBD) are placed in a suitable fashion in order to intercept the different particles. The signal from the SBD, proportional to the energy deposited by the impinging particles, is amplified and analyzed using pulse height discrimination. The output of the discriminator is fed into a multichannel scaler (MCS) that is triggered at the start of each machine cycle. The MCS records the signal as a function of time. By simply relating the time delay to energy, one can record the signal as a function of the CM energy. An experimental difficulty is that the detection of the events resulting from a given process and the ion current measurement require very different ion beam intensities. Indeed, a relatively low ion beam current is needed in order to avoid pile-up in the SBD, whereas the measurement of the ion beam current requires an intense ion beam to get a statistically acceptable recording. This problem is solved by relating the SBD and current transformer signals to the recording from the scintillator detector. The experimental rate coefficient at a given CM energy is given by

$$\langle v_{rel}\sigma \rangle = R_B \frac{C}{n_e\, l} \frac{N}{N_{Scint}} \tag{7}$$

In this expression, C is the circumference of the ring, l is the length of the interaction region and n_e is the electron density. N is the difference between the number of counts obtained with the collision energies set to E_{cool} (with velocity matched electrons) and E_{cm}. Simultaneously, another independent MCS spectrum, labeled N_{Scint}, is recorded with the scintillation detector. The last parameter in Eq. (7), R_B, is the destruction rate per ion. It can be derived from another MCS spectrum taken with the same scintillation detector, but acquired at the same time as the ion current measurement, I_i. This is given by

$$R_B = \frac{dN_{Scint}}{dt} \frac{1}{I_i} f\, e, \tag{8}$$

where *f* represents the orbital frequency of the ions in the ring.

The cross sections can be extracted from the corresponding rate coefficients using the Fourier transform technique mentioned above. Specific experimental difficulties that must be solved include: trapped ions in the cooler section, the spread in the collision energies and the contribution to the signal from the so-called "toroidal" regions of the electron cooler.[8]

3.2 Branching Fractions

3.2.1 Grid

Many neutral fragments can arise from the open dissociation channels. The counts detected by the SBD are recorded along with the energy of a "neutral event" (combination of neutrals) that occurs at a specific fraction of the full ion beam energy. Since many open channels may contribute to this same "neutral event", these channels are therefore, not distinguishable from each other. To remove this indetermination, one can make use of a grid that is placed in front of the energy-sensitive SBD. This grid is thick enough to stop all neutral fragments that do not pass through the grid holes. If the transmission probability for passage of a neutral fragment through a hole is T, then the absorption probability is (1-T). Since particles stopped by the grid are not recorded by the SBD, the counts originating from a specific "neutral event" (when the grid is not inserted) are redistributed among "neutral events" characterized by smaller fraction of the total ion beam energy. A set of linear equations can be constructed, which relate the number of dissociation events in the different open channels N_i, to the measured numbers of counts in the various "neutral events" N_{meas} that correspond to specific fractions of the full ion beam energy. The final result can be summarized by the following set of equations:

$$[N_{meas}] = [M][N_i], \tag{9}$$

with the transmission matrix, [M]. By solving this matrix equation, one can extract the branching ratios. The critical value of the grid transmission was recently carefully reanalyzed[7] and was found to be 0.297 (± 0.015).

3.2.2 Imaging detector

A position sensitive imaging detector can be used in order to record the distance separation between DR fragments.[5, 9] This detector is positioned 6.3 meters beyond the interaction region, in the zero degree section. DR fragments strike the first of a package of three multichannel plates (MCPs; 77 mm in diameter), the signal from which produces flashes on a phosphor screen. The light is detected by a CCD (Charge Coupled Device) camera that is used to image the fragment separations. The kinetic energy shared among the fragments can be determined and the dissociation limits can be identified. Moreover, a photo-multiplier tube is used as an event trigger in order to grab the image from the CCD camera and to reduce the high voltage (250 V/100 ns) over the MCP package by means of a fast switch. This is used to identify false coincidences in the camera frames. A background spectrum is measured separately. The data can be reduced using the following formula, which

applies for an individual distance distribution and a given kinetic energy release (the finite length of the interaction region is also taken into account):

$$P(D) = \frac{1}{D_{L+1/2} - D_{L-1/2}} \left(\cos^{-1}\left(\min\left(1, \frac{D}{D_{L+1/2}}\right)\right) - \cos^{-1}\left(\min\left(1, \frac{D}{D_{L-1/2}}\right)\right)\right). \quad (10)$$

L is the distance to the center of the cooler (6.3 m) and l denotes the length of the interaction region (0.85 m). The maximum distance separations of the fragments when the dissociation occurs at the beginning of the cooler and at the end are $D_{L+l/2}$ and $D_{L-l/2}$, respectively.

4. CN^+

The cyanogen cation CN^+ can be found in the hot, high-density conditions, existing in flames.[3] One of its destruction pathways is the DR mechanism:[10-11]

$$CN^+(X^1\Sigma^+, v=0) + e^- \rightarrow C(^3P) + N(^4S) + 6.3 \text{ eV} \quad (11a)$$
$$\rightarrow C(^1D) + N(^4S) + 5.0 \text{ eV} \quad (11b)$$
$$\rightarrow C(^3P) + N(^2D) + 3.9 \text{ eV} \quad (11c)$$
$$\rightarrow C(^1S) + N(^4S) + 3.6 \text{ eV} \quad (11d)$$
$$\rightarrow C(^3P) + N(^2P) + 2.7 \text{ eV} \quad (11e)$$
$$\rightarrow C(^1D) + N(^2D) + 2.6 \text{ eV} \quad (11f)$$
$$\rightarrow C(^5S) + N(^4S) + 2.1 \text{ eV} \quad (11g)$$
$$\rightarrow C(^1D) + N(^2P) + 1.4 \text{ eV} \quad (11h)$$
$$\rightarrow C(^1S) + N(^2D) + 1.2 \text{ eV} \quad (11i)$$
$$\rightarrow C(^1S) + N(^2P) + 0.0 \text{ eV} \quad (11j)$$

The ions were produced in a conventional ion source, from a mixture of nitrogen and methane in a 9 to 1 ratio. The 12 s lower limit for the $a^3\Pi$ radiative lifetime, comparable to the 6s delay between injection of the beam and data acquisition, means that our measurement refers to a CN^+ beam which is a mixture of the $X^1\Sigma^+$ and $a^3\Pi$ states. An additional 0.08 eV would have to be added to all of the exothermicities mentioned above in order to get those for $CN^+(a^3\Pi, v = 0)$. For the $X^1\Sigma^+$ state, we obtain vibrational relaxation times of 38, 58 and 115 ms for the v = 3, v = 2 and v = 1 levels, respectively, and the equivalent quantities for the $a^3\Pi$ state are 101, 152 and 304 ms. Therefore, our measurement refers to vibrationally cold ions.

4.1 Experimental Findings

Fig. 3(a) displays the deconvoluted cross sections. We have found[11] a steeper cross section energy dependence over the range from 0.4 to 3 eV of:

$$\sigma(E_{cm}) = 1.49 \times 10^{-15} (0.4/E_{cm})^{1.41} \quad (12)$$

than that expected from the so-called direct process, i.e. E^{-1}, which is observed below 0.1 eV :

$$\sigma(E_{cm}) = 8.00 \times 10^{-14} (0.01/E_{cm})^{1.05} \quad (13)$$

The branching fractions were obtained after subtraction of the background contribution to the signal, by fitting each distance distribution spectrum with a linear combination of the individual distance distributions for a given Kinetic Energy Release, KER (see Eq. (10)). Moreover, we had to account for the presence of the $a^3\Pi$ state. Because of the small energy gap between the KER values corresponding to the $C(^3P)+N(^2D)/C(^1S)+N(^4S)$, $C(^3P)+N(^2P)/C(^1D)+N(^2D)$ and $C(^1D)+N(^2P)/C(^1S)+N(^2D)$ limits, it is not possible to give individual final state branching fractions for all of the products. This limitation is due to the spatial resolution of our detector. The distribution of distances measured at 0 eV CM energy is shown in Fig. 4. At this energy, the DR process yields only a small percentage of ground state atomic fragments (< 1.8 % $C(^3P)+N(^4S)$). The second most exothermic limit $C(^1D)+N(^4S)$ is not significantly populated either (3.8 %). The main contributing channels come in pairs, namely the $C(^3P)+N(^2D)/C(^1S)+N(^4S)$, $C(^3P)+N(^2P)/C(^1D)+N(^2D)$ and $C(^1D)+N(^2P)/C(^1S)+N(^2D)$ limits that account for 14.2, 56.1 and 25.5 %, respectively. The $C(^5S)+N(^4S)$ channel as well as the less exothermic $C(^1S)+N(^2P)$ channel were not found to be significantly populated (< 1 - 1.4 %, respectively).

4.2 Interpretation and Discussion

For the direct DR process to be efficient at low energies, there must be a favorable crossing of a repulsive neutral curve through the lower part of the ionic curve. Among the nine neutral curves[15] that are displayed in Fig. 5, not all are suitable to drive the DR via the direct process. The curves labeled $D^2\Pi i$, $E^2\Sigma^+$ or $^2\Pi(4)$ do not intersect the ionic curves near their minima. Two additional factors indicate that these states do not contribute significantly to the recombination of CN^+. The energy dependence at low energy is very close to the E_{cm}^{-1} dependence, which is the signature of the direct process and more persuasively, the dissociation limits for these states are not observed to be populated in our branching fraction measurements. For the ground state ion, we have found that the best Franck-Condon overlap is achieved with the state labeled $^2\Sigma^+(5)$. This state has the most favorable curve crossing with the ion, since it cuts the $X^1\Sigma^+$ state at the bottom of the potential well. For the $a^3\Pi$ state, we have found that the best overlap is achieved with the states labeled $^2\Sigma^+(6)$ and $^2\Pi(6)$. These findings are supported by the branching results, since it was shown that 81.6 % of the dissociating flux goes to the $C(^3P)+N(^2P)$, $C(^1D)+N(^2D)$, $C(^1D)+N(^2P)$ and $C(^1S)+N(^2D)$ limits. On the

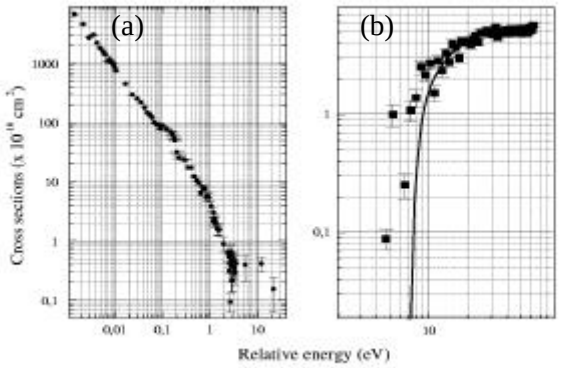

Figure 3. (a) DR cross sections as derived from the measured rate coefficients, using a deconvolution procedure.[3] (b) Electron impact detachment cross sections for CN^-.[12] The data points are the experimental data, and the solid line is a fit to the semi-classical model.[13, 14]

other hand, we have found that the "paired" limits $C(^3P)+N(^2P)/C(^1D)+N(^2D)$ are more populated than the $C(^1D)+N(^2P)/C(^1S)+N(^2D)$ limits. This certainly means that some of the other states from Fig. 5 contribute significantly to the DR process, especially those converging to the $C(^3P)+N(^2P)$ and $C(^1D)+N(^2D)$ limits (such as the $^2\Sigma^+(4)$ and $^2\Pi(5)$ states). The less exothermic $C(^1S)+N(^2P)$ channel is not found to be significantly populated. The exothermicity for this channel is indeed very small. A dissociative state of the CN molecule converging to this asymptotic limit and displaying a favorable curve crossing near the v = 0 of the ion, would have to be extremely shallow.

5. CN^-

Particular interest in the CN^- anion is associated with its relatively high degree of stability against detachment, with an electron affinity of 3.8 eV. This anion can readily form tightly bound complexes with several transition metal ions,[17] and it can also be used to dope alkali halide crystals in lattice defect studies.[18] CN^- ions were produced in a cesium sputter ion source[19] with a cathode made of boron nitride (BN) and graphite. An important issue is the internal excitation of the target anions. In particular, the $a^3\Pi$ excited state is expected to be long-lived since the $a^3\Pi \rightarrow X^1\Sigma^+$ transition is spin forbidden. The calculated lifetime, 21 ms, is small compared with the storage time of the CN^- ions in the storage ring, several seconds. Therefore, the internal state of the CN^- ions in our beam was exclusively the $^1\Sigma^+$ electronic ground state. It was also important to evaluate the different relaxation times for the vibrational levels of this state. We estimated lifetimes of 700, 930,

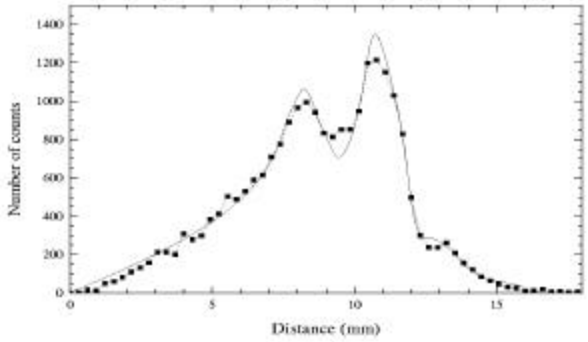

Figure 4. Distance spectrum for the branching fraction determination. The (--) symbol shows experimental data taken at 0 eV CM energy whereas the full drawn line shows a best fit to the experimental data. The scale is 0.31 mm per pixel.

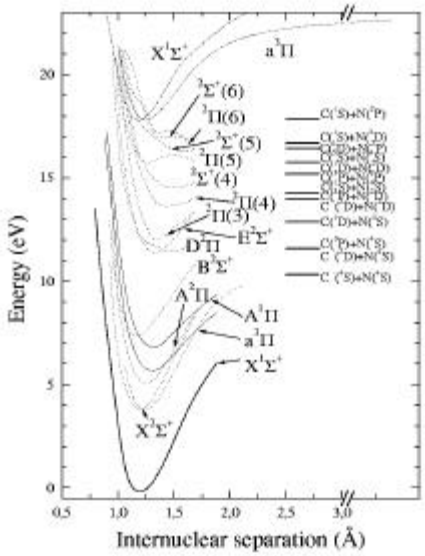

Figure 5. Potential energy curves relevant to the CN,[15] CN^+,[16] and CN^- [26] studies. The ten asymptotic limits are represented.

1390 and 2790 ms for the levels v = 4, 3, 2 and 1, respectively. We therefore conclude that our measurements refer to $CN^-(X^1\Sigma^+, v=0,1)$ anions.

Over the energy range that was investigated, several channels had to be considered:

$$CN^- + e- \rightarrow CN + 2e \quad (14a)$$
$$\rightarrow C^- + N + e \quad (14b)$$
$$\rightarrow C + N + 2e \quad (14c)$$
$$\rightarrow C + N^+ + 3e \quad (14d)$$
$$\rightarrow C^+ + N + 3e \quad (14e)$$
$$\rightarrow CN^+ + 3e \quad (14f)$$
$$\rightarrow C^- + N^+ + 2e \quad (14g)$$
$$\rightarrow C^+ + N^+ + 4e \quad (14h)$$

An experimental complication arose from the fact that the energy sensitive SBD that was used to record the neutral fragments cannot distinguish between the channel 14a and 14c. To overcome this difficulty, we made use of a grid placed in front of the detector as described above.

5.1 Experimental Findings

A branching ratio measurement was made at a CM energy of 60 eV: 91(±4)% was found to branch into the pure detachment channel, (14a), and 8(±4)% into the dissociation channel C^- + N (14b). The flux into all other open channels represents less than 1%, but none were large enough separately to warrant quoting an accurate value. In Fig. 3(b), we present the measured cross section curve for the pure detachment channel, (14a), over the electron energy range 0-60 eV. The overall shape of the curve shows an onset at a threshold energy of about 7 eV. This threshold is determined by the binding energy of the anion (3.8 eV) plus a finite contribution due to the Coulomb repulsion. The cross section then increases monotonically up to a maximum around 25 eV followed by a plateau with at $\sim 5 \times 10^{-16}$ cm^2.

5.2 Interpretation and Discussion

The $^3\Pi$ and $^1\Pi$ states, which are displayed in Fig. 5, correlate to $C^-(^2D)$ + $N(^4S)$ and $C^-(^2D)$ + $N(^2D)$ dissociation channels, respectively. Other curves (not shown here), corresponding to different molecular symmetries and multiplicities, also correlate to these two dissociation limits (34 in total). Moreover, three other Σ^+ states of different multiplicities correlate to the limit $C^-(^4S)$ + $N(^4S)$, in addition to the $^1\Sigma^+$ ground state.[26] Concerning the neutral states, it must be stressed that these curves, relevant to the DR process, are adapted from Lavendy et al.[15] who did not consider symmetries other than Σ^+ and Π. The omitted symmetries include those of Σ^-, Δ, Φ and Γ character that account for 13, 13, 5 and 1 of the molecular states, respectively (over a total of 73 neutral states and ten asymptotes). One might notice that of the thirteen calculated[15] Σ^+ and Π states, nine of them are the lowest bound states of the neutral CN radical. In fact, among the overall 73 states, a majority of them are expected to be associated with bound states. Many states can, in principle,

be reached by electron collisions. For example, consider the neutral states produced in the electron detachment of molecular anions. The neutrals can further stabilize by radiative decay. The upper $^2\Sigma^+$ (5, 6) and $^2\Pi$ (6) states of CN, as displayed in Fig. 5, could very well contribute to the very weak observed dissociation channel 14c. As mentioned earlier, a total of 40 anionic potential curves correlate to the three lowest anionic limits. Electron impact excitation from CN^- ($X^1\Sigma^+$, v=0,1) can generate the $a^3\Pi$ and $A^1\Pi$ states. The population of these excited states would radiatively decay to the $^1\Sigma^+$ ground state with lifetimes of 21 ms and 269 ns, respectively. Of course, this process of pure excitation cannot be studied in a storage ring, since the excited CN^- anions will continue to circulate in the ring. This process might, however, significantly affect states other than the three bound anionic states displayed in Fig. 5. A purely repulsive anionic state might certainly contribute to the 8(±4)% of the flux that we measured for the dissociative channel $C^- + N$ (14b).

We now turn to the second issue that we attempted to address in this work, namely the search for the possible existence of a doubly charged anion that should have appeared as a near-threshold resonance in the detachment curve. The full line in Fig. 3(b) represents a fit to our experimental data at medium energy, using a semi-classical formalism.[13,14] In a comparison of this fit and our data in the energy range 7-11 eV, one might notice an obvious discrepancy. This structure could imply the existence of a dianionic resonance in this region, but the statistical uncertainty in the experiment was, however, too large to either prove or disprove the existence of such a resonance. It is interesting to note that the CN^{-2} ion is unable to correlate at large internuclear separations to $C^- + N^-$, since N has a negative electron affinity. The resonance might be associated with a virtual state of CN^{-2}. Such a short lived state would perhaps explain why the observed structure is broad.

6. HCN^+/HNC^+

The MEIBE apparatus was used to examine the DR of [C-H-N^+] ions.[2] HCN^+ is an interesting ion because of its isomerisation chemistry. Ab initio calculations have indicated that the HCN^+ ion has a $^2\Pi$ ground state and is less stable by 0.98eV[20] than HNC^+, which has a $^2\Sigma^+$ ground state. Petrie et al.[21] have found that, after electron impact upon HCN, the relative concentration of HCN^+ and HNC^+ ground states are in the ratio of approximately 3 to 1. They showed that addition of carbon dioxide leads to a plasma that is completely dominated by HNC^+. It was also observed[22] that HCN^+ reacts rapidly with CH_4 but HNC^+ does not.

We carried out different sets of measurements, using different gas mixtures:

- *8.35% N_2 – 8.35% CH_4 – 83.3% CO_2.* The ion beam was comprised primarily of HNC^+ ions (96.2%). The HCN^+ population accounted for the remaining 3.8%.[23]
- *90% N_2 - 10% CH_4*. The HCN^+ population (12.5%) was more significant than with the above mixture but HNC^+ (87.5%)[23] remained the overwhelmingly populated isomer.

One has not only to question the possible presence of isomeric forms [C-H-N^+] in the target beam, but also their internal excitation. The $B^2\Sigma^+$ and $A^2\Sigma^+$ HCN^+ states lie 5.25 and 0.40eV above the $X^2\Pi$ state,[24] respectively. It is likely that the X and A states were populating our target beam since the HCN^+ A state radiative lifetime is 3ms. The $B^2\Sigma^+$ and $A^2\Pi$ HNC^+ states lie 10.63 and 2.13eV above $X^2\Sigma^+$ HNC^+,[25] respectively. Only the X state was likely to be populated in our target beam since HNC^+ A state has a much shorter radiative lifetime than that of its HCN^+ counterpart.

At 0 eV CM energy, three dissociation channels are open for ground state HNC^+ ions:

$$HNC^+ + e \rightarrow CN + H + 7.2eV, \quad (15a)$$
$$\rightarrow NH + C + 3.9eV, \quad (15b)$$
$$\rightarrow CH + N + 2.9eV, \quad (15c)$$

and four for HCN^+:

$$HCN^+ + e \rightarrow CN + H + 8.2eV, \quad (16a)$$
$$\rightarrow NH + C + 4.9eV, \quad (16b)$$
$$\rightarrow CH + N + 3.9eV, \quad (16c)$$
$$\rightarrow H + C + N + 0.4eV. \quad (16d)$$

6.1 Experimental Findings

The cross sections are plotted in Fig. 6 over the range 1meV - 1eV.[2] The filled squares are for the target beam produced from the N_2/CH_4 source gas mixture. The open circles represent the data points taken under the $N_2/CH_4/CO_2$ mixture. The two sets of cross sections exhibit the same general trend, except in the 0.01-0.04eV and 0.1-0.3eV energy range. It appears that the HCN^+ DR process is considerably more efficient than that for HNC^+; the cross sections for HCN^+/HNC^+ being systematically larger than for HNC^+ "alone".

6.2 Interpretation and Discussion

We carried out a quantum chemical investigation of the DR of $HCN^+(X^2\Pi)$, $HNC^+(X^2\Sigma^+)$ and $HCN^+(A^2\Sigma^+)$.[23] Only the most thermodynamically favorable CN+H exit channels were considered. The relevant curves that drive the DR of $HCN^+(X^2\Pi$ and $A^2\Sigma^+)$ are displayed in Fig. 7(a) in the

quasi-diabatic representation. There is a crossing between the lowest $1D^1\Pi$ dissociative state and the lowest $^{1,3}\Pi$ Rydberg states at their minima. Similarly, the lowest $1D^{1,3}\Sigma$ dissociative states intersect the lowest $^{1,3}\Sigma$ Rydberg states at the minima of the Rydberg curves. No curve crossing is observed between the ionic $X^2\Pi$, $A^2\Sigma^+$ and any of the dissociative $^{1,3}\Pi$ or lowest dissociative $^{1,3}\Sigma$ states. However, there is a higher repulsive state, $2D^3\Sigma$ that crosses both HCN^+ $X^2\Pi$ and $A^2\Sigma^+$ at their minima.

The curves governing the DR of HNC^+ ($X^2\Sigma^+$) can be seen in Fig. 7(b) in the quasi-diabatic representation. The lowest repulsive state $1D^3\Sigma$ crosses the lowest Rydberg state of similar multiplicity at its minimum energy arguing for an efficient DR via the indirect mechanism. Similarly, the repulsive states $1D^1\Pi$ and $1D^3\Pi$, cross the lowest $^1\Pi$ and $^3\Pi$ Rydberg states at their minima. The second repulsive state, $2D^3\Sigma$, crosses the ion curve. This crossing occurs at the third vibrational energy level of HNC^+.

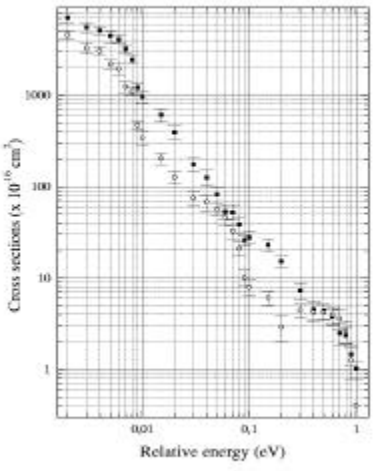

Figure 6. DR cross sections for the isomeric mixture HCN^+/HNC^+ (full squares) and for HNC^+ "alone" (open circles).

Fig. 7(a) suggests that the DR of HCN^+ ($X^2\Pi$ and $A^2\Sigma^+$) could involve both the direct and indirect mechanisms. The direct process where the $X^2\Pi$ and $A^2\Sigma^+$ states of HCN^+ together with the neutral repulsive state $HCN(2D^3\Sigma)$ will be involved and the indirect process where $^1\Pi$ Rydberg states together with the $1D^1\Pi$ dissociative state and $^{1,3}\Sigma$ Rydberg states together with $1D^{1,3}\Sigma$ will be involved. Fig. 7(b) suggests that the DR of HNC^+ ($X^2\Sigma^+$, v=0) will involve an indirect mechanism, but that for HNC^+ ($X^2\Sigma^+$,v=2) will proceed via the direct mechanism. Usually, the

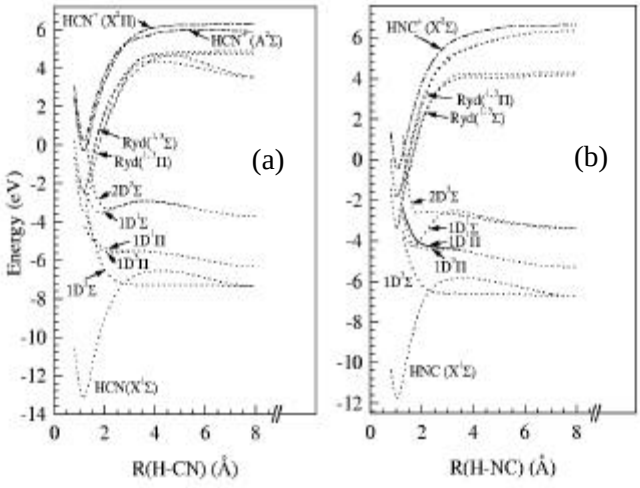

Figure 7. (a) Σ and Π HCN quasi-diabatic potential energy curves. (b) Σ and Π HNC quasi-diabatic curves. Energies are in atomic units and distances in Angstroms.

indirect DR process is less efficient than the direct one and our present results are in perfect agreement with this picture. Indeed, we extracted the DR thermal rates for pure HCN^+ and HNC^+ from the cross sections displayed in Fig. 6, and the HCN^+ rate is found to be about 28 times larger than that for HNC^+.

7. CONCLUSION

The DR of $CN^+(X^1\Sigma^+$ and $a^3\Pi$, v=0) is efficient, in agreement with the findings made for other diatomic ions. Cross sections of about $1.0x10^{-12}$ cm^2 at 1 meV and $1.0x10^{-14}$ cm^2 at 1 eV are found, with essentially a E_{cm}^{-1} dependence. The experimental results from the imaging detector indicate that at zero collision energy, the DR mechanism is dominated by a direct dissociation process which does not populate the ground state limit $C(^3P)+N(^4S)$. Concerning CN^-, we have measured cross sections for single detachment. The cross section rose from zero at threshold to a maximum of about $5x10^{-16}$ cm^2 just below 30 eV, after which it remained essentially constant up to about 60 eV. A slight enhancement of the cross section in the threshold region may be due to the presence of a resonance associated with the doubly charged negative ion CN^{-2}.

Two different source mixtures were used in order to study the DR of the isomeric HCN^+/HNC^+ ions: N_2-CH_4 (90-10%) to obtain HCN^+/HNC^+ ions in a 12.5/87.5% proportion and CO_2-N_2-CH_4 (85%-13.5%-1.5%) to obtain a

beam containing predominantly HNC^+ with a 3.8/96.2% proportion. We have found that the DR rate coefficient of the isomer HCN^+ is much larger than that for the HNC^+ isomer, though the process is efficient for both cases.

ACKNOWLEDGMENTS

The author wants to express his gratitude to Mats Larsson and his group, to Brian Mitchell, to Dahbia Talbi as well as to Dag Hanstorp.

REFERENCES

1 C. J. Keyser, H. R. Froelich, J. B. A. Mitchell and W. J. McGowan, J. Phys. E: Sci. Instr. **12,** 316 (1979).
2 C. Sheehan, A. Le Padellec, W. N. Lennard, D. Talbi and J. B. A. Mitchell, J. Phys. B **32,** 3347 (1999).
3 J. R. Mowat, H. Danared, G. Sundström, M. Carlson, L. H. Andersen, L. Vejby-Christensen, M. af Ugglas and M. Larsson, Phys. Rev. Lett. **74,** 50 (1995).
4 A. Al-Khalili, H. Danared, M. Larsson, A. Le Padellec, R. Peverall, S. Rosén, J. Semaniak, M. af Ugglas, L. Vikor and W. van der Zande, Hyper. Int. **114,** 281 (1998).
5 S. Rosén, R. Peverall, M. Larsson, A. Le Padellec, J. Semaniak, Å. Larson, C. Strömholm, W. van der Zande, H. Danared and G. H. Dunn, Phys. Rev. A **57,** 4462 (1998).
6 S. Rosén, A. M. Derkatch, J. Semaniak, A. Neau, A. Al-Khalili, A. Le Padellec, L. Vikor, H. Danared, M. af Ugglas, R. Thomas and M. Larsson, Faraday Discuss. **115**, 295 (2000).
7 A. Neau, A. Al-Khalili, S. Rosén, J. Semaniak, A. Le Padellec, A. M. Derkatch, W. Shi, L. Vikor, M. Larsson, R. Thomas, M. Nagard, K. Andersson, H. Danared and M. af Ugglas, J. Chem. Phys. **113**, 1762 (2000).
8 A. Lampert, A. Wolf, D. Habs, J. Kettner, G. Kilgus, D. Schwalm, M. S. Pindzola and N. R. Badnell, Phys. Rev. A **53**, 1413 (1996).
9 D. Zajfman, Z. Amitay, C. Broude, P. Forck, B. Seidel, M. Grieser, D. Habs, D. Schwalm, and A. Wolf, Phys. Rev. Lett. **75**, 814 (1995).
10 A. Le Padellec, C. Sheehan and J.B.A. Mitchell, J. Phys. B **31**, 1725 (1998).
11 A. Le Padellec, J. B. A Mitchell, A. Al-Khalili, H. Danared, A. Källberg, Å. Larson, S. Rosén, M. af Ugglas, L. Vikor and M. Larsson, J. Chem. Phys. **110**, 890 (1999).
12 A. Le Padellec, K. Andersson, D. Hanstorp, F. Hellberg, M. Larsson, A. Neau, S. Rosén, H. T. Schmidt, R. Thomas, J. Semaniak, D. J. Pegg, F. Österdahl, H. Danared and A. Källberg, Phys. Script. **64**, 467 (2001).
13 L. H. Andersen, D. Mathur, H. T. Schmidt and L. Vejby-Christensen, Phys. Rev. Lett. **74**, 892 (1995).
14 L. Vejby-Christensen, D. Kella, D. Mathur, H. B. Pedersen, H. T. Schmidt and L. H. Andersen, Phys. Rev. A **53**, 2371 (1996).
15 H. Lavendy, G. Gandara and J. M. Robbe, J. Mol. Spectr. **106**, 395 (1984).
16 D. M. Hirst, Mol. Phys. **82**, 359 (1994).
17 F. A. Cotton and G. Wilkinson, "Advanced Inorganic Chemistry", (Wiley-Interscience, New York, 1972).

18 B. M. Chadwick and H. G. M. Edwards, "Molecular Spectroscopy", Vol. 1, (Chemical Society, London, 1972).
19 Peabody Scientific, Peabody, Massachusetts, USA.
20 K. A. Peterson, R. C. Mayrhofer and R. C. Woods, J. Chem. Phys. **93,** 4946 (1990).
21 S. Petrie, C. G. Freeman, M. Meot-Ner, M. J. McEwan and E. E. Ferguson , J. Am. Chem. Soc. **112,** 7121 (1990).
22 S. Petrie, C. G. Freeman, M. J. McEwan and E. E. Ferguson, Mon. Not. R. Astron. Soc. **248,** 272 (1991).
23 D. Talbi, A. Le Padellec and J. B. A. Mitchell, J. Phys. B **33**, 3631 (2000).
24 C. Fridh and J. Asbrink, J. Electron Spectrosc. Relat. Phenom. **7,** 119 (1975).
25 D. Forney, W. E. Thompson and M. E. Jacox, J. Chem. Phys. **97,** 1664 (1992).
26 T.K. Ha and G. Zumofen, Mol. Phys. **40**, 445 (1980).